Research article

Qingyu Tian[a], Peng Yin[a], Teng Zhang, Lunbin Zhou, Bin Xu*, Zhengqian Luo, Hongliang Liu*, Yanqi Ge*, Jian Zhang, Peng Liu and Xiaodong Xu

MXene $Ti_3C_2T_x$ saturable absorber for passively Q-switched mid-infrared laser operation of femtosecond-laser–inscribed Er:Y_2O_3 ceramic channel waveguide

https://doi.org/10.1515/nanoph-2020-0005
Received January 3, 2020; revised January 24, 2020; accepted January 24, 2020

Abstract: We report on an Er:Y_2O_3 ceramic channel waveguide laser operating at continuous-wave and passively Q-switched regimes, for the first time to the best of our knowledge. The Er:Y_2O_3 ceramic channel waveguide has been fabricated by a femtosecond laser direct-writing technique. The maximum output power reached 123.5 mW in continuous-wave mode with a slope efficiency of about 21%, and the lasing behavior has been found simultaneously at 2710.28, 2716.76, and 2723.18 nm. We have further fabricated an MXene $Ti_3C_2T_x$ saturable absorber mirror to operate the Er:Y_2O_3 waveguide in passively Q-switched regime. At the same time, property of the MXene $Ti_3C_2T_x$ saturable absorber has been characterized, and nonlinear saturable absorption of the saturable absorber has also been measured. The average output power is about 67.6 mW, and the shortest pulse width is about 58.1 ns. This work indicates that femtosecond laser direct writing is a reliable technique for processing mid-infrared ceramic waveguides, and MXene $Ti_3C_2T_x$ is promising for operating pulsed mid-infrared lasers.

Keywords: MXene $Ti_3C_2T_x$ saturable absorber; waveguide; mid-infrared; passive Q switching.

1 Introduction

Optical waveguide, a well-known integrated optical device, allows a small spot size and hence a high intensity because of the confinement of light inside a waveguide. If the waveguide is doped with an active laser ion, then extremely low laser thresholds can be achieved, provided the waveguide loss is low, which is compatible with high-beam-quality but low-power laser diode pumping. Rare-earth–doped waveguide lasers are always indispensable for the development of compact coherent light sources. The development trend has been accelerated in recent years, thanks to the promotion of a novel waveguide fabrication technique, namely, femtosecond (fs) laser direct writing [1, 2], which is a simple and flexible technique for waveguide fabrication. Because of nonlinear absorption processes, a focalized fs-laser pulse can produce modifications at micrometric or submicrometric scales, thus inducing changes of the refractive index inside the material.

In fact, the fs-laser–writing technique is now widely recognized as a powerful tool for realizing waveguides in various transparent optical materials [2–22]. During the past decade, fs-laser–inscribed Pr^{3+} [3–5], Nd^{3+} [6–11], Yb^{3+} [12–14], Er^{3+} [15], Tm^{3+} [16–18], Ho^{3+} [19, 20], and Cr^{2+} [21, 22] waveguide lasers have been demonstrated. However, in terms of laser emission wavelength, it is obvious that these waveguide lasers have still been limited at shorter than about 2.5 μm. Researches on mid-infrared (MIR) waveguide lasers have been really very rarely studied. Mid-infrared wavelength has important applications in remote-sensing technology, atmospheric-environment monitoring, and especially in biomedical science, because of their strong water absorption and the penetration depth of a few microns in biological tissue.

[a]**Qingyu Tian and Peng Yin:** These authors contributed equally to this work.
***Corresponding author: Bin Xu,** Department of Electronic Engineering, Xiamen University, Xiamen 361005, China, e-mail: xubin@xmu.edu.cn. https://orcid.org/0000-0003-0960-6140; **Hongliang Liu,** Institute of Modern Optics, Nankai University, Tianjin 300350, China, e-mail: drliuhl@nankai.edu.cn; and **Yanqi Ge,** College of Optoelectronic Engineering, Shenzhen University, Shenzhen 518060, China, e-mail: geyanqi@szu.edu.cn
Qingyu Tian, Teng Zhang, Lunbin Zhou and Zhengqian Luo: Department of Electronic Engineering, Xiamen University, Xiamen 361005, China. https://orcid.org/0000-0002-2800-8472 (Z. Luo)
Peng Yin: College of Optoelectronic Engineering, Shenzhen University, Shenzhen 518060, China
Jian Zhang: Key Laboratory of Transparent and Opto-functional Inorganic Materials, Shanghai Institute of Ceramics, Chinese Academy of Sciences, No. 588 Heshuo Road, Shanghai 201899, China
Peng Liu and Xiaodong Xu: Jiangsu Key Laboratory of Advanced Laser Materials and Devices, School of Physics and Electronic Engineering, Jiangsu Normal University, Xuzhou 221116, China

Open Access. © 2020 Bin Xu, Hongliang Liu et al., published by De Gruyter. This work is licensed under the Creative Commons Attribution 4.0 Public License.

Unauthenticated
Download Date | 2/12/20 6:19 PM

Pulsed operation based on passively Q-switched or mode-locked technology via saturable absorber (SA) has greatly extended the application of laser sources. Semiconductor SA mirror (SESAM), as one of the representative conventional SAs, has gained significant success during the past decades. However, introducing such conventional SAs into waveguide laser cavities will lead to the compactness destruction [23]. Monolithic waveguide structure by incorporating conventional SA inside a waveguide needs complicated waveguide fabrication technology [24]. Moreover, SESAMs need complex semiconductor fabrication process, and therefore, they are quite expensive. Additionally, they only work at specific and narrow wavelength ranges with bandwidths of about several tens of nanometer. Saturable absorbers based on two-dimensional (2D) materials have now become a popular research topic because they have great advantages such as cost efficiency, easy fabrication, and broadband absorption. Many 2D-materials SAs have been developed for diode-pumped solid-state lasers (DPSSLs) [25–32] and fiber lasers [33–42] in the recent several years.

The problems that SESAM suffers for operating a waveguide laser can now be perfectly solved by using these 2D-materials SAs. Two-dimensional materials in the form of thin film made from liquid phase exfoliation or chemical vapor deposition method can be very conveniently and readily transferred onto the surface of waveguide or output coupler (OC) and serve as SAs. For instance, graphene [16, 43, 44], Bi_2Se_3 [45], WS_2 [46], black phosphorous [46], $MoSe_2$ [47], WSe_2 [47], $PtSe_2$ [48], and graphene/WS_2 heterostructure [10] have been demonstrated for pulsed waveguide lasers.

Recently, MXene, a graphene-like layered material, has attracted considerable attention due to its strong storage capacity, tunable bandgap, broad optical response, and good conductivity [49–52]. Moreover, its remarkable nonlinear saturable absorption has also been applied for pulsed laser generation from visible to MIR wavelengths [52–58]. Such broadband absorption property is very attractive, and more novel pulsed laser sources could be realized based on MXene SA. In this work, Er:Y_2O_3 ceramic has been fabricated into a channel waveguide via fs-laser–writing technique. Based on this Er:Y_2O_3 ceramic waveguide platform, we have operated the first Er^{3+}-doped MIR waveguide laser using MXene $Ti_3C_2T_x$ SA.

2 Waveguide fabrication

Waveguide fabrication setup is shown in Figure 1. A Ti:sapphire regenerative amplifier (Astrella; Coherent, Santa Clara, CA, USA), which delivers 800-nm pulses with a tunable duration of 35 to 120 fs and a maximum pulse energy of 6 mJ at a repetition rate of 1 kHz, is employed to fabricate cladding structures buried inside the ceramic. In the laser-writing process, the incident laser beam is focused through the largest crystal facet (5×7 mm^2) at a maximum depth of 250 μm by a 40× microscope objective (N.A. = 0.65). The crystal wafer is placed on a motorized six-dimensional micropositioning stage (ALIO AI-HH-60XY-15Z-56R), which allows for precise translation of the sample at a constant velocity ~1.5 mm/s, which can minimize the stress effect induced by laser pulses. A pulse energy of 2 μJ with a pulse duration of 80 fs (on sample) is identified as the optimal value in order to produce laser-damage tracks while avoiding crystal cracking. Under our experimental conditions, a damage track with a vertical length of 8 μm and a lateral width of 1.5 μm can be produced via a single scan. A number of parallel scans are performed, with a constant lateral separation of 3 μm, at different depths beneath the crystal surface to define a single-cladding waveguide with radius of about 60 μm. All the waveguides are written along the 7-mm-long edge of the sample. With choosing these fs-laser inscription parameters, efficient guiding and lasing features can be achieved with low losses during the pumping experiment.

3 Fabrication and characterization of MXene SA

The few-layer MXene nanoflakes were prepared by the acid-etching process. The starting material can be Ti_3AlC_2, and its powder (98%, 200 mesh; Forsman Scientific Co., Beijing, China) was first ground in an agate mortar for

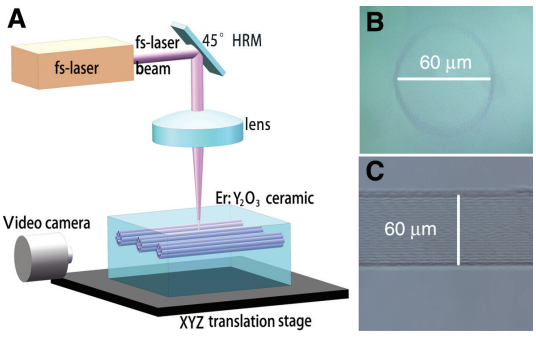

Figure 1: Experimental setup of femtosecond laser direct writing and optical microscope images of the waveguide.
(A) The schematic of femtosecond laser direct writing in an Er:Y_2O_3 ceramic waveguide. (B and C) Optical microscope images of the as-fabricated waveguide cross sections with diameters of about 60 μm.

Unauthenticated
Download Date | 2/12/20 6:19 PM

30 min with manual operation in condition of di-ionic water. The resulting miscible liquids were added into 40 wt% hydrofluoric (HF) acid according to the volume ratio of 1:12. After exfoliation with a magnetic stirrer at 48°C for 12 h, the resulting deposition was scoured by di-ionic water up to pH > 6 and dried for 8 h in a vacuum drying oven in condition of 80°C. The *N*-methyl-2-pyrrolidone (NMP) of 1 mg/ml was used to dissolve the MXene powder because of its strong surface tension of ~40 mN/ml. Finally, the centrifugal operation was introduced for 30 min with speed of ~5000 revolutions/min, to acquire the stratified suspension with precipitated MXene particles and supernatant as the few-layer MXene nanosheets NMP solution.

In MXene $Ti_3C_2T_x$, the two layers of carbon atoms can be located in three layers of titanium atoms generating representative ABC stacking order in hexagonal crystal lattices. The typical accordion-like shapes of exfoliated $Ti_3C_2T_x$ explicitly appear in Figure 2A, by a scanning electron microscope based on a JEOL JSM- 7000F electron microscope (Shanghai, China) after the acid-etching operation. Because of the small scale, the gaps in accordion-like shapes were also observed clearly. In order to study the morphology of the prepared 2D MXene, transmission electron microscopy (TEM) (Figure 2B) technique was applied using an FEI Tecnai F20 instrument (Hillsboro, OR, USA). Several MXene $Ti_3C_2T_x$ nanosheets with various

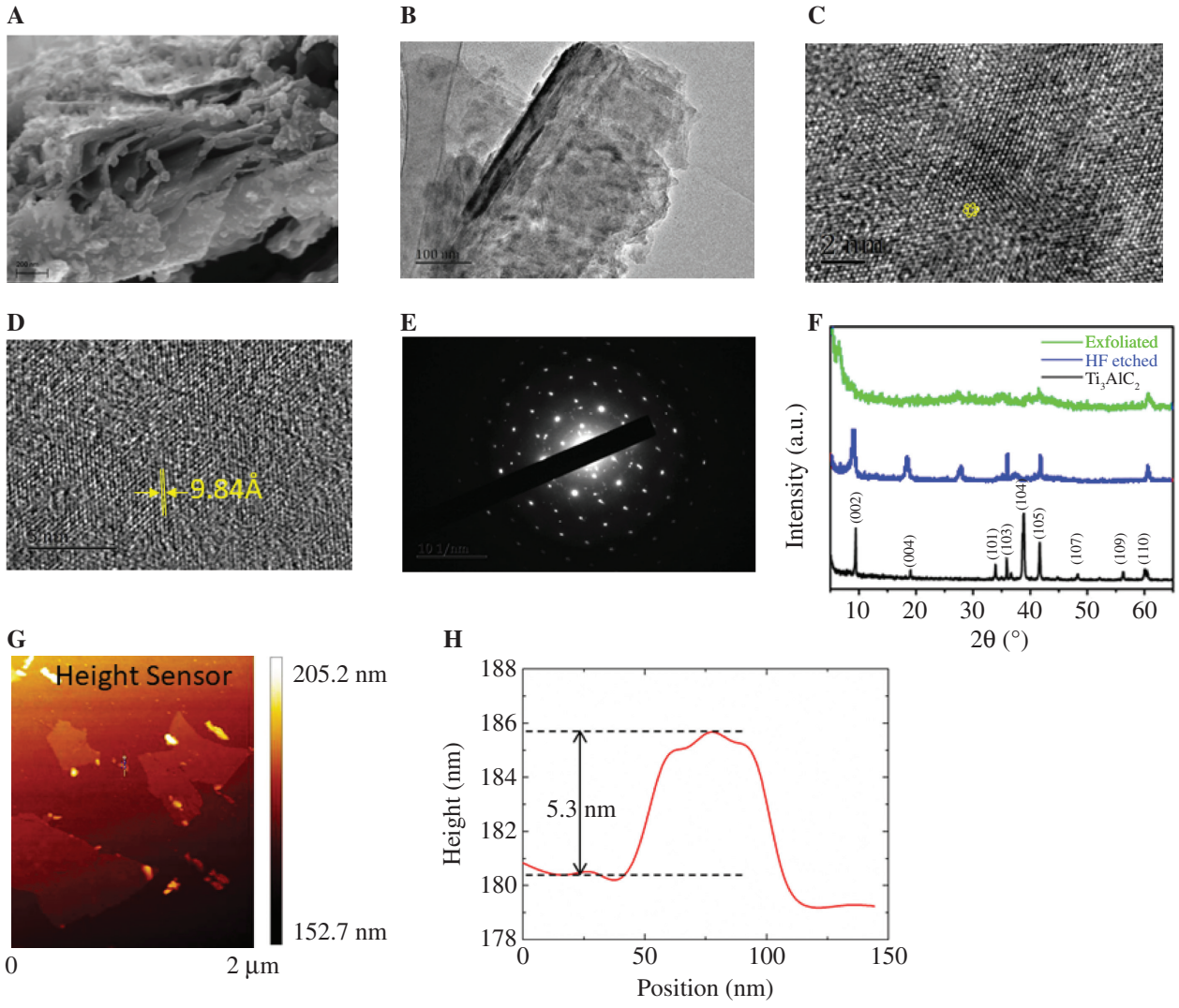

Figure 2: Characterizations of the synthesized MXene $Ti_3C_2T_x$ nanosheets.
(A) scanning electron microscope images of exfoliated $Ti_3C_2T_x$ after HF etching; (B) typical TEM image of exfoliated few-layer $Ti_3C_2T_x$ with the scale bar of 100 nm; (C) high-resolution transmission electron microscopy (HRTEM) image of atomic lattice of $Ti_3C_2T_x$; (D) The HRTEM pattern of the nanosheet and the interlayer distance is tested to be 9.84Å; (E) typical selected area electron diffraction (SAED) pattern of the $Ti_3C_2T_x$ nanosheet; (F) X-ray diffraction (XRD) pattern of the sample: before HF treatment, after HF treatment, and exfoliated nanosheets; (G) representative atomic force microscope topographic image and (H) the corresponding height profile.

Unauthenticated
Download Date | 2/12/20 6:19 PM

thicknesses "bunched up" together, while the as-prepared MXene $Ti_3C_2T_x$ nanosheets can be easily selected because of being very thin and transparent to electrons with monolayer film of hundreds of nanometers. The crystal lattice of the 2D MXene $Ti_3C_2T_x$ is shown in Figure 2C after zoom in the TEM image. The regular hexagon shape can be observed clearly. The high-resolution TEM pattern of the nanosheet is shown in Figure 2D, and the interlayer distance is tested to be 9.84Å. In addition, typical selected area electron diffraction pattern of the $Ti_3C_2T_x$ nanosheet is shown in Figure 2E. The hexagonal symmetry of the as-prepared MXene $Ti_3C_2T_x$ nanosheets can be seen. Figure 2F shows the X-ray diffraction (XRD) pattern where the black, blue, and green lines depict the starting Ti_3AlC_2, HF-etched Ti_3AlC_2, and exfoliated $Ti_3C_2T_x$, respectively. The XRD patterns were recorded on PANalytical X'Pert X-ray diffractometer (Eindhoven, The Netherlands) equipped with Cu-Kα radiation using 40-kV accelerating voltage and 40-mA applied current. The increase in the c-LP can be observed because of the transformation from MAX to MXene, in which case the (001) peaks heighten and transfer to lower angles. At the location of 6.8 degrees, the XRD pattern of the HF-etched Ti_3AlC_2 shows a quite feeble, wide peak. A stronger broad peak, at a similar 2θ, is the strongest peak in the $Ti_3C_2T_x$ pattern (green line), showing a shift of the (002) peak from 2θ = 9 degree to 6.8 degree, corresponding to the c-LPs of 23 Å to 28 Å for Ti_3AlC_2 and $Ti_3C_2T_x$, respectively. Because of the poor alignment of the thin MXene films, the (002) peak of exfoliated $Ti_3C_2T_x$ is also feeble and wide. Figure 2G shows the atomic force microscope image of the as-prepared $Ti_3C_2T_x$ MXene nanosheets on the Si/SiO_2 substrates. The slice profile of the $Ti_3C_2T_x$ MXene nanosheets can be observed and measured. Figure 2H depicts the corresponding profile of the $Ti_3C_2T_x$ MXene nanosheets, which indicates the thickness of one nanosheet can be about 5.3 nm.

Nonlinear saturable absorption of the SA was measured using a homemade MIR pulsed laser source based on diode-pumped passively Q-switched Er:YSGG solid-state laser emitting at about 2.79 μm. This laser source has a pulse width of about 12 ns and pulse repetition rate of about 45 kHz. The measured nonlinear saturable absorption of the MXene SA is shown in Figure 3. The laser source has an M^2 factor of about 1.6, and it has been focused to a beam waist of about 70 μm, which leads to a Rayleigh length of about 3.44 mm. According to the formula that associates transmittance and incident optical intensity,

$$T = 1 - \frac{a_s}{1 + I/I_s} - a_{ns} \quad (1)$$

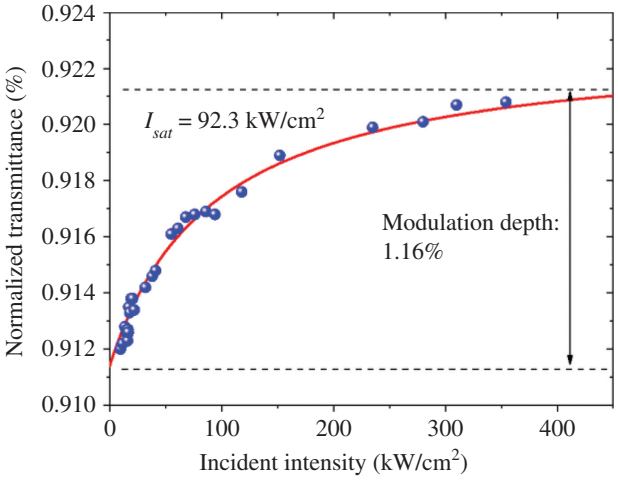

Figure 3: Nonlinear saturable absorption data and its corresponding fitting curve.

where α_s is the modulation depth, α_{ns} is the nonsaturable loss, and I_s is the saturable intensity. By fitting the experimental data, these parameters have been found to be about 1.16%, 7.7%, and 92.3 kW/cm^2, respectively.

4 Experimental setup

The waveguide laser experimental setup is schematically shown in Figure 4. A 976-nm diode laser was coupled into an optical fiber pigtail with core diameter of 25 μm and numerical aperture of 0.1, which served as pump source in the experiments. The pump beam was collimated by a 30-mm (focal length) doublet lens and then was focused by another 60-mm doublet lens. Thus, the two optical coupling doublet lenses lead to a pump spot size of about 50 μm, which allows the injection of the pump beam into the waveguide with 60-μm core diameter. In order to lessen reflection loss, front surface of the waveguide was antireflection coated at pumping wavelength and lasing wavelength. The waveguide was enclosed into a copper

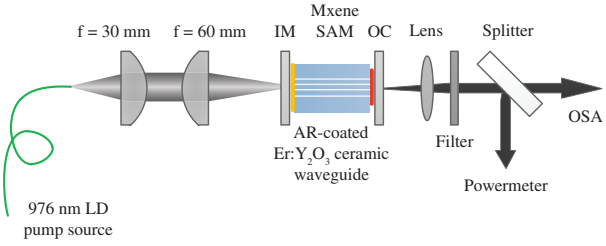

Figure 4: The schematic of Er:Y_2O_3 ceramic channel waveguide laser experiment.

Unauthenticated
Download Date | 2/12/20 6:19 PM

block and then fixed on a five-dimensional fine mount, without extra cooling.

The 1-mm-thick flat input mirror made from CaF_2 has a high transmission of 94% at pumping wavelength and high reflection of more than 99.8% at lasing wavelengths. The OC has a transmission of about 4.8% at lasing wavelength. The $Ti_3C_2T_x$ SA has been fabricated by transferring the dispersion onto the OC via a spin-coating method. The two cavity mirrors are butt-coupled to the waveguide ends, as shown in Figure 4. The laser output is collimated by a positive lens for various measurements after a filter for removing the residual pump light.

5 Experimental results

For laser experiments, the as-inscribed waveguide has been repolished to remove the improperly inscribed ends. After a good alignment of the waveguide cavity, continuous-wave (CW) laser operation was achieved by using a part of the OC that has no $Ti_3C_2T_x$ thin film. Figure 5 shows the output power variation with increase in the absorbed pump power. The threshold is about 155 mW, and the maximum output power reached 123.5 mW. Moreover, the measured output power exhibits good linearity with slope efficiency of about 21%. At maximum output power, beam spot showing the intensity profile of the output laser is shown as insets in Figure 5. The present maximum output power was only limited by the available pump power. Therefore, power scaling could be possible simply by increasing the pump power in the near future.

The inset in Figure 5 shows the waveguide laser emitting at 2710.28, 2716.76, and 2723.18 nm, simultaneously, in CW mode. According to the emission spectrum of Er:Y_2O_3 ceramic [59], $^4I_{11/2}\rightarrow{}^4I_{13/2}$ emission of this material has four dominant emission peaks at 2710, 2717, 2723, and 2739 nm with emission cross sections pretty close to each other. Therefore, here it is not strange that we have obtained simultaneous tri-wavelength lasing, with the only 2739-nm emission excluded, which indeed has the smallest cross section, relatively. In fact, previously, we have already obtained simultaneous dual-wavelength laser in bulk Er:Y_2O_3 ceramic crystal [60]. Therefore, here in this work, the tri-wavelength lasing could be owing to a higher gain for the active medium being in the form of waveguide. Moreover, compared with the bulk laser, the waveguide laser with high gain also leads to far smaller threshold (155 vs. 801 mW) and higher efficiency (21% vs. 11.8%), except the pump-power–limited maximum output power. By the way, to our knowledge, this is the first demonstration of tri-wavelength Er^{3+} MIR laser. In addition, the output power stability of the tri-wavelength laser was measured to be about 3.4% in 20 min, as shown in Figure 6.

Using a simple Findlay–Clay analysis, we can estimate the intracavity round-trip loss L by using the following expression:

$$\eta_s = \frac{\lambda_p}{\lambda_o}\eta_p\frac{T}{T+L} \tag{2}$$

where η_s is the slope efficiency; λ_p is the pumping wavelength; λ_o is the laser wavelength; η_p is the excitation quantum efficiency, i.e. the fraction of excited ions per

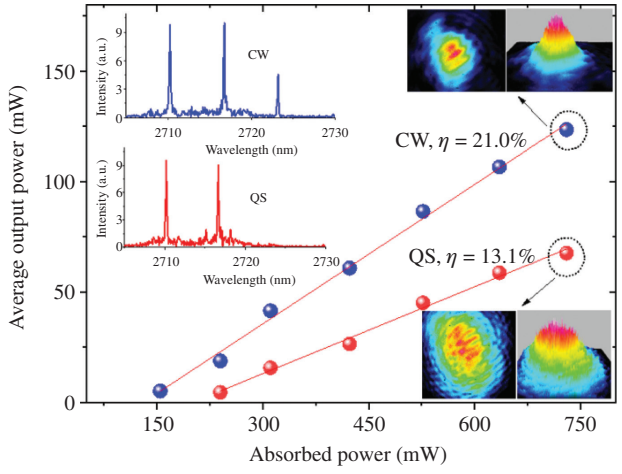

Figure 5: The average output power dependence on absorbed power in CW and QS modes; insets: the corresponding laser wavelengths and the laser beam spots at maximum output powers.

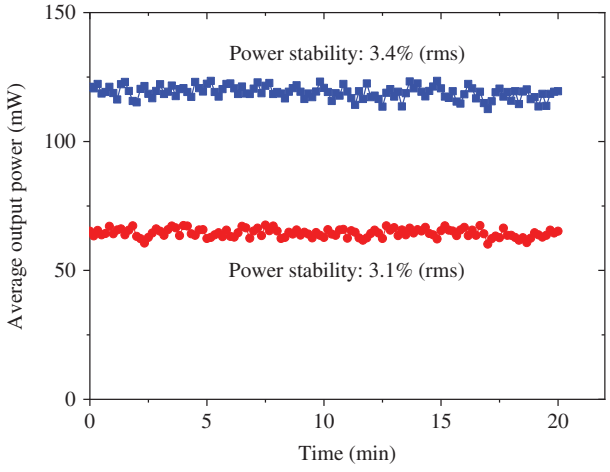

Figure 6: The laser output power stabilities under CW and passively Q-switched regimes.

Unauthenticated
Download Date | 2/12/20 6:19 PM

absorbed pump photons, which can be assumed to be equal to unity as the concentration quenching should not be significant considering the moderate concentration of the used laser gain medium; T is the transmission of OCs; and L is the intracavity round-trip loss. Substituting the relevant parameter values into this expression, we can readily calculate the intracavity round-trip loss to be about 3.3%. The relatively not small loss should be mainly ascribed to fabricating quality of the waveguide itself if we neglect the losses originating from end-face mirrors and coating. Further optimizing the waveguide quality for improving the waveguide laser performance will be carried out in the near future.

Moving the $Ti_3C_2T_x$ SA mirror perpendicularly to the cavity axis allowed us flexibly operating the waveguide laser in CW or Q-switched regime. As doing so, passively Q-switched waveguide laser has also been operated with a maximum average output power of 67.6 mW, as shown in Figure 5. The laser threshold increased to about 240 mW, and the slope efficiency decreased to 13.1%. The laser spectrum shows the lasing behavior occurred at 2710.19 and 2716.67 nm, simultaneously. The 2723-nm emission has been suppressed probably due to the larger intracavity loss under the passively Q-switched regime. Moreover, we measured the stability of pulsed laser to be about 3.1%, comparable to the CW case.

In Figure 7, we report the single pulse profile at maximum output power with a full width at half maximum (FWHM) of about 58.1 ns. Under this situation, the pulse trains show a repetition rate of 1.98 MHz (see the inset in Figure 7). The output laser was found to be 100% modulated as no residual CW component can be observed from the oscilloscope. Moreover, we observed that the pulse trains showed good stability with similar intensities. We further measured intensity instability of the pulse trains at maximum output power to be less than about 8.9%. The temporal instability was also observed with timing jitter of less than about 9 ns.

Modulation depth of the used $Ti_3C_2T_x$ SA can be further estimated according to the following theoretical equation for a passively Q-switched laser operation [61]:

$$a_s = 3.52\frac{t_r}{\tau} \tag{3}$$

where α_s is still the modulation depth of the SA, t_r is the cavity round-trip time, and τ is the achieved pulse width. Using this formula, we can simply calculate the modulate depth to be a little less than 1%, which is quite close to the above measurement value. Anyway, the relatively small modulation depth could be the main factor that limited further pulse width narrowing. Hence, optimizing the SA for higher modulation depth, shorter pulse width of the passively Q-switched $Er:Y_2O_3$ ceramic waveguide laser could be expected in the future.

In Figure 8, we show the dependence of pulse width and pulse repetition rate on absorbed power. At threshold, pulse width was about 126.5 ns, and it decreased almost linearly to the minimum. The pulse repetition rate shows a reverse variation trend as it showed a minimum value of about 1.02 MHz at threshold and then increased to the maximum, monotonously. According to these parameter values, we can simply estimate the pulse energy and pulse peak power at corresponding absorbed power. As shown in Figure 9, pulse energy was about 4.5 nJ, and pulse peak power was 36 mW at threshold, and then they both monotonously increased to 34 nJ and 588 mW, respectively.

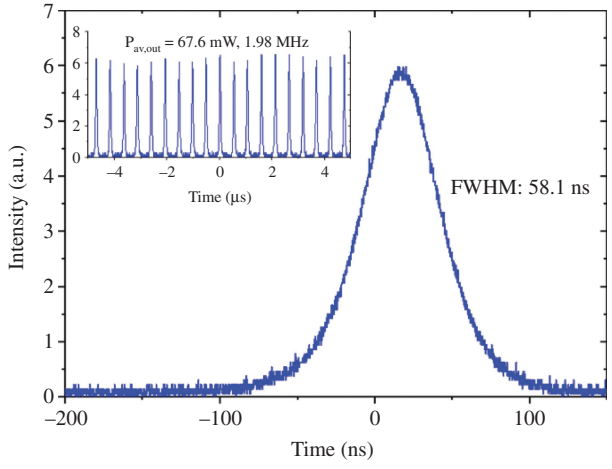

Figure 7: The single pulse profile showing a pulse time duration of about 58.1 ns; inset: pulse trains at maximum output power with repetition rate of 1.98 MHz.

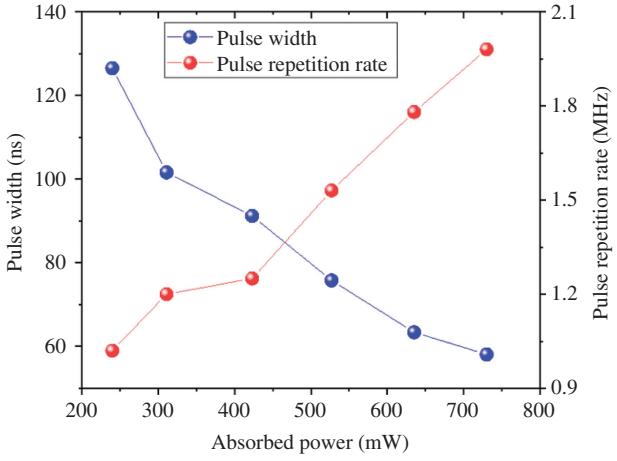

Figure 8: The pulse width and pulse repetition rate varying with absorbed power.

Unauthenticated
Download Date | 2/12/20 6:19 PM

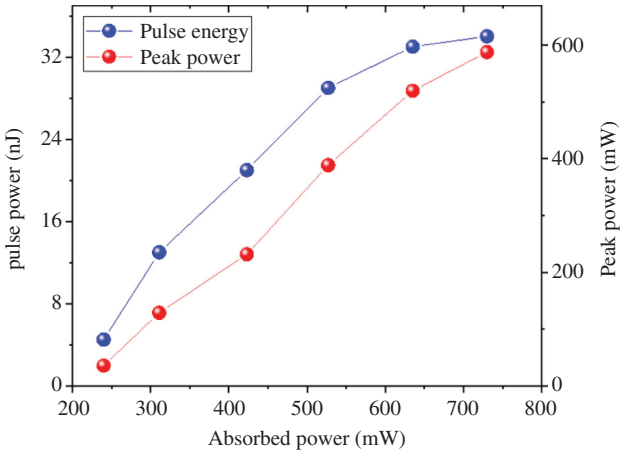

Figure 9: The pulse energy and pulse peak power varying with absorbed power.

6 Conclusion

An Er:Y_2O_3 ceramic channel waveguide based on fs-laser direct-writing method has been fabricated for operating an MIR waveguide laser. The maximum output power reached 123.5 mW in CW mode, while the average output power reduced to 67.6 mW when the waveguide was operated in passively Q-switched regime with an MXene $Ti_3C_2T_x$ SA mirror. The achieved shortest pulse width is about 58.1 ns, which is indeed a very narrow time duration for 2D-materials SAs.

This work indicates that the novel MXene $Ti_3C_2T_x$ is promising for operating MIR waveguide lasers. Passive mode locking of the Er:Y_2O_3 ceramic waveguide laser could be realized by inscribing the waveguide structure to smaller radius, e.g. to the scale of about 10 μm [62], for promoting the intracavity pulse energy. In addition, we believe that pulsed waveguide lasers, like 2D-materials–based fiber laser and DPSSLs, will develop greatly in the near future with the fast rising of more and more novel and outstanding 2D materials [63–69].

Acknowledgments: This work is supported by the National Natural Science Foundation of China (61575164, 61575088, Funder Id: http://dx.doi.org/10.13039/501100001809); the Natural Science Foundation of Fujian Province of China (2018J01108); the International Collaborative Laboratory of 2D Materials for Optoelectronics Science and Technology, Shenzhen University (2DMOST2018026); and the Fundamental Research Funds for the Central Universities (20720180057).

Competing interests: The authors declare no competing interests.

References

[1] Davis KM, Miura K, Sugimoto N, Hirao K. Writing waveguides in glass with a femtosecond laser. Opt Lett 1996;21:1729–31.
[2] Gattass RR, Mazur E. Femtosecond laser micromachining in transparent materials. Nat Photonics 2008;2:219–25.
[3] Calmano T, Siebenmorgen J, Reichert F, et al. Crystalline Pr:$SrAl_{12}O_{19}$ waveguide laser in the visible spectral region. Opt Lett 2011;36:4620–22.
[4] Müller S, Calmano T, Metz P, Hansen NO, Kränkel C, Huber G. Femtosecond-laser–written diode-pumped Pr:$LiYF_4$ waveguide laser. Opt Lett 2012;37:5223–5.
[5] Liu HL, Luo SY, Xu B, et al. Femtosecond-laser micromachined Pr:YLF depressed cladding waveguide: raman, fluorescence, and laser performance. Opt Mater Express 2017;7:3990–7.
[6] Okhrimchuk AG, Shestakov AV, Khrushchev I, Mitchell J. Depressed cladding, buried waveguide laser formed in a YAG:Nd^{3+} crystal by femtosecond laser writing. Opt Lett 2005;30:2248–50.
[7] Calmano T, Siebenmorgen J, Hellmig O, Petermann K, Huber G. Nd:YAG waveguide laser with 1.3 W output power, fabricated by direct femtosecond laser writing. Appl Phys B 2010;100:131–5.
[8] Ren Y, Dong N, Macdonald J, Chen F, Zhang HJ, Kar AK. Continuous wave channel waveguide lasers in Nd:$LuVO_4$ fabricated by direct femtosecond laser writing. Opt Express 2012;20:1969–74.
[9] Salamu G, Jipa F, Zamfirescu M, Pavel N. Laser emission from diode-pumped Nd:YAG ceramic waveguide lasers realized by direct femtosecond-laser writing technique. Opt Express 2014;22:5177–82.
[10] Li Z, Cheng C, Dong N, et al. Q-switching of waveguide lasers based on graphene/WS_2 van der Waals heterostructure. Photonic Res 2017;5:406–10.
[11] Wu PF, He S, Liu HL. Annular waveguide lasers at 1064 nm in Nd:YAG crystal produced by femtosecond laser inscription. Appl Opt 2018;57:5420–4.
[12] Ams M, Dekker P, Marshall GD, Withford MJ. Monolithic 100 mW Yb waveguide laser fabricated using the femtosecond-laser direct-write technique. Opt Lett 2009;34:247–9.
[13] Calmano T, Paschke AG, Siebenmorgen J, et al. Characterization of an Yb:YAG ceramic waveguide laser, fabricated by the direct femtosecond-laser writing technique. Appl Phys B 2011;103:1–4.
[14] Ma L, Tan Y, Wang SX, et al. Continuous-wave and Q-switched Yb:YSGG waveguide laser. J Lightwave Technol 2017;35:2642–5.
[15] Taccheo S, Della Valle G, Osellame R, et al. Er:Yb-doped waveguide laser fabricated by femtosecond laser pulses. Opt Lett 2004;29:2626–8.
[16] Ren YY, Brown G, Mary R, et al. 7.8-GHz graphene-based 2-μm monolithic waveguide laser. IEEE J Sel Top Quant 2015;21:1602106.
[17] Morris J, Stevenson NK, Bookey HT, et al. 1.9 μm Waveguide laser fabricated by ultrafast laser inscription in Tm:Lu_2O_3 ceramic. Opt Express 2017;25:14910–7.
[18] Kifle E, Mateos X, Aldana JRV, et al. Femtosecond-laser–written Tm:$KLu(WO_4)_2$ waveguide lasers. Opt Lett 2017;42:1169–71.
[19] McDaniel S, Thorburn F, Lancaster A, Stites R, Cook G, Kar A. Operation of Ho:YAG ultrafast laser inscribed waveguide lasers. Appl Opt 2017;56:3251–6.

Unauthenticated
Download Date | 2/12/20 6:19 PM

[20] Kifle E, Loiko P, Romero C, et al. Femtosecond-laser–written Ho:KGd$(WO_4)_2$ waveguide laser at 2.1 μm. Opt Lett 2019;44:1738–41.
[21] Macdonald JR, Beecher SJ, Lancaster A, et al. Compact Cr:ZnS channel waveguide laser operating at 2333 nm. Opt Express 2014;22:7052–7.
[22] Macdonald JR, Beecher SJ, Berry PA, Brown G, Schepler KL, Kar AK. Efficient mid-infrared Cr:ZnSe channel waveguide laser operating at 2486 nm. Opt Lett 2013;38:2194–6.
[23] Bolaños W, Carvajal JJ, Mateos X, et al. Continuous-wave and Q-switched Tm-doped KY$(WO_4)_2$ planar waveguide laser at 1.84 μm. Opt Express 2011;19:1449–54.
[24] Beach RJ, Mitchell SC, Meissner HE, et al. Continuous-wave and passively Q-switched cladding-pumped planar waveguide lasers. Opt Lett 2001;26:881–3.
[25] Feng TL, Zhao SZ, Yang KJ, et al. Diode-pumped continuous wave tunable and graphene Q-switched Tm:LSO lasers. Opt Express 2013;21:24665–70.
[26] Cafiso SDD, Ugolotti E, Schmidt A, et al. Sub-100-fs Cr:YAG laser mode-locked by monolayer graphene saturable absorber. Opt Lett 2013;38:1745–7.
[27] Xu B, Cheng Y, Wang Y, et al. Passively Q-switched Nd:$YAlO_3$ nanosecond laser using MoS_2 as saturable absorber. Opt Express 2014;22:28934–40.
[28] Xu B, Wang Y, Peng J, et al. Topological insulator Bi_2Se_3 based Q-switched Nd:$LiYF_4$ nanosecond laser at 1313 nm. Opt Express 2015;23:7674–80.
[29] Ma J, Xie GQ, Zhang J, Yuan P, Tang DY, Qian LJ. Passively mode-locked Tm:YAG ceramic laser based on graphene. IEEE J Sel Top Quant 2015;21:1100806.
[30] Kong LC, Xie GQ, Yuan P, et al. Passive Q-switching and Q-switched mode-locking operations of 2 μm Tm:CLNGG laser with MoS_2 saturable absorber mirror. Photonic Res 2015;3:A47–50.
[31] Guan X, Wang J, Zhang Y, et al. Self-Q-switched and wavelength-tunable tungsten disulfide-based passively Q-switched Er:Y_2O_3 ceramic lasers. Photonic Res 2018;6:830–6.
[32] Liu JJ, Huang H, Zhang F, et al. Bismuth nanosheets as a Q-switcher for a mid-infrared erbium-doped SrF_2 laser. Photonic Res 2018;6:762–5.
[33] Bao Q, Zhang H, Wang Y, et al. Atomic-layer graphene as a saturable absorber for ultrafast pulsed lasers. Adv Funct Mater 2009;19:3077–83.
[34] Zhang H, Tang DY, Zhao LM, Bao QL, Loh KP. Large energy mode locking of an erbium-doped fiber laser with atomic layer graphene. Opt Express 2009;17:17630–5.
[35] Sun Z, Hasan T, Torrisi F, et al. Graphene mode-locked ultrafast laser. ACS Nano 2010;4:803–10.
[36] Luo Z, Zhou M, Weng J, et al. Graphene-based passively Q-switched dual-wavelength erbium-doped fiber laser. Opt Lett 2010;35:3709–11.
[37] Luo AP, Zhu PF, Liu H, et al. Microfiber-based, highly nonlinear graphene saturable absorber for formation of versatile structural soliton molecules in a fiber laser. Opt Express 2014;22:27019–24.
[38] Woodward RI, Howe RCT, Hu G, et al. Few-layer MoS_2 saturable absorbers for short-pulse laser technology: current status and future perspectives. Photonic Res 2015;3:A30–9.
[39] Chen Y, Jiang G, Chen S, et al. Mechanically exfoliated black phosphorus as a new saturable absorber for both Q-switching and mode-locking laser operation. Opt Express 2015;23:12823–8.
[40] Luo Z, Wu D, Xu B, et al. Two-dimensional material-based saturable absorbers: towards compact visible-wavelength all-fiber pulsed lasers. Nanoscale 2016;8:1066.
[41] Liu M, Luo AP, Xu WC, Luo ZC. Dissipative rogue waves induced by soliton explosions in an ultrafast fiber laser. Opt Lett 2016;41:3912–4.
[42] Wang J, Jiang Z, Chen H, et al. High energy soliton pulse generation by a magnetron-sputtering-deposition–grown $MoTe_2$ saturable absorber. Photonic Res 2018;6:535–8.
[43] Mary R, Brown G, Beecher SJ, et al. 1.5 GHz picosecond pulse generation from a monolithic waveguide laser with a graphene-film saturable output coupler. Opt Express 2013;21:7943–8.
[44] Choudhary A, Dhingra S, D'Urso B, et al. Q-switched operation of a pulsed-laser–deposited Yb:Y_2O_3 waveguide using graphene as a saturable absorber. Opt Lett 2014;39:4325–8.
[45] Tan Y, Zhang H, Zhao CJ, Akhmadaliev S, Zhou SQ, Chen F. Bi_2Se_3 Q-switched Nd:YAG ceramic waveguide laser. Opt Lett 2015;40:637–40.
[46] Tan Y, Guo Z, Ma L, et al. Q-switched waveguide laser based on two dimensional semiconducting materials: tungsten disulfide and black phosphorous. Opt Express 2016;24:2858–63.
[47] Cheng C, Liu HL, Tan Y, Aldana JR, Chen F. Passively Q-switched waveguide lasers based on two-dimensional transition metal diselenide. Opt Express 2016;24:10385–90.
[48] Li Z, Li R, Pang C, et al. 8.8 GHz Q-switched mode-locked waveguide lasers modulated by $PtSe_2$ saturable absorber. Opt Express 2019;27:8727–32.
[49] Jiang X, Liu S, Liang W, et al. Broadband nonlinear photonics in few-layer MXene $Ti_3C_2T_x$ (T=F, O, or OH). Laser Photonic Rev 2018;12:1700229.
[50] Dong Y, Chertopalov S, Maleski K, et al. Saturable absorption in 2D Ti_3C_2 MXene thin films for passive photonic diodes. Adv Mater 2018;30:1705714.
[51] Wang C, Wang Y, Jiang X, et al. MXene $Ti_3C_2T_x$: a promising photothermal conversion material and application in all-optical modulation and all-optical information loading. Adv Opt Mater 2019;7:1900060.
[52] Jhon YI, Koo J, Anasori B, et al. Metallic MXene saturable absorber for femtosecond mode-locked lasers. Adv Mater 2017;29:1702496.
[53] Feng XY, Ding BY, Liang WY, et al. MXene $Ti_3C_2T_x$ absorber for a 1.06 μm passively Q-switched ceramic laser. Laser Phys Lett 2018;15:085805.
[54] Wu Q, Jin X, Chen S, et al. MXene-based saturable absorber for femtosecond mode-locked fiber lasers. Opt Express 2019;27:10159–65.
[55] Li J, Zhang Z, Du L, et al. Highly stable femtosecond pulse generation from a MXene $Ti_3C_2T_x$ (T=F, O, or OH) mode-locked fiber laser. Photonic Res 2019;7:260–3.
[56] Zu Y, Zhang C, Guo X, et al. A solid-state passively Q-switched Tm,Gd:CaF_2 laser with a $Ti_3C_2T_x$ MXene absorber near 2 μm. Laser Phys Lett 2019;16:015803.
[57] Hao Q, Liu J, Zhang Z, et al. Mid-infrared Er:CaF_2–SrF_2 bulk laser Q-switched by MXene $Ti_3C_2T_x$ absorber. Appl Phys Express 2019;12:085506.
[58] Yang Q, Zhang F, Zhang N, Zhang H. Few-layer MXene $Ti_3C_2T_x$ (T=F, O, or OH) saturable absorber for visible bulk laser. Opt Mater Express 2019;9:1795–9.

Unauthenticated
Download Date | 2/12/20 6:19 PM

[59] Sanamyan T, Simmons J, Dubinskii M. Er^{3+}-doped Y_2O_3 ceramic laser at ~2.7μm with direct diode pumping of the upper laser level. Laser Phys Lett 2010;7:206–9.
[60] Guan X, Zhan L, Zhu Z, et al. Continuous-wave and chemical vapor deposition graphene-based passively Q-switched Er:Y_2O_3 ceramic lasers at 2.7 um. Appl Opt 2018;57:371–6.
[61] Spuhler GJ, Paschotta R, Fluck R, et al. Experimentally confirmed design guidelines for passively Q-switched microchip lasers using semiconductor saturable absorbers. J Opt Soc Am B 1999;16:376–88.
[62] Li R, Pang C, Li Z, et al. Monolithic waveguide laser mode-locked by embedded Ag nanoparticles operating at 1 μm. Nanophotonics 2019;8:859–68.
[63] Xie Z, Xing C, Huang W, et al. Ultrathin 2D nonlayered tellurium nanosheets: facile liquid-phase exfoliation, characterization, and photoresponse with high performance and enhanced stability. Adv Funct Mater 2018;28:1705833.
[64] Xie Z, Zhang F, Liang Z, et al. Revealing of the ultrafast third-order nonlinear optical response and enabled photonic application in two-dimensional tin sulfide. Photonic Res 2019;7:494–502.
[65] Wu L, Xie Z, Lu L, et al. Few-layer tin sulfide: a promising black-phosphorus analogue 2D material with exceptionally large nonlinear optical response, high stability, and applications in all-optical switching and wavelength conversion. Adv Optical Mater 2018;6:1700985.
[66] Xing C, Xie Z, Liang Z, et al. 2D nonlayered selenium nanosheets: facile synthesis, photoluminescence, and ultrafast photonics. Adv Optical Mater 2017;5:1700884.
[67] Huang W, Xie Z, Fan T, et al. Black-phosphorus-analogue tin monosulfide: an emerging optoelectronic two-dimensional material for high-performance photodetection with improved stability under ambient/harsh conditions. J Mater Chem C 2018;6:9582–93.
[68] Xing C, Huang W, Xie Z, et al. Ultrasmall bismuth quantum dots: facile liquid-phase exfoliation, characterization, and application in high-performance UV-Vis photodetector. ACS Photonics 2018;5:621–9.
[69] Xie Z, Chen S, Duo Y, et al. Biocompatible two-dimensional titanium nanosheets for multimodal imaging-guided cancer theranostics. ACS Appl Mater Interfaces 2019;11:22129–40.

Unauthenticated
Download Date | 2/12/20 6:19 PM